Chemical Engineering Journal 392 (2020) 123737

Contents lists available at ScienceDirect

Chemical Engineering Journal

journal homepage: www.elsevier.com/locate/cej

Synthesis and characterization of $Nd(OH)_3$-ZnO composites for application in photocatalysis and disinfection

Sabryna I.G. Costa[a], Vinícius D. Cauneto[a], Leila D. Fiorentin-Ferrari[a], Priscila B. Almeida[b], Regiane C. Oliveira[c], Elson Longo[b], Aparecido N. Módenes[a], Veronice Slusarski-Santana[a,*]

[a] Program of Post-Graduation in Chemical Engineering, State University of West Parana, P.O. Box 520, Toledo 85903-000, PR, Brazil
[b] CDMF, LIEC, Federal University of São Carlos, P.O. Box 676, São Carlos 13565-905, SP, Brazil
[c] Modeling and Molecular Simulations Group, São Paulo State University, UNESP, 17033-360 Bauru, SP, Brazil

HIGHLIGHTS

- Composites combining $Nd(OH)_3$ and ZnO were synthesized.
- Synergic effect between $Nd(OH)_3$ and ZnO favored photocatalytic activity.
- $1Nd(OH)_3$-ZnO composite showed high antimicrobial activity against *E. coli* and *S. aureus*.
- $Nd(OH)_3$-ZnO can be used as luminescent materials, photocatalyst and antibacterial agent.

GRAPHICAL ABSTRACT

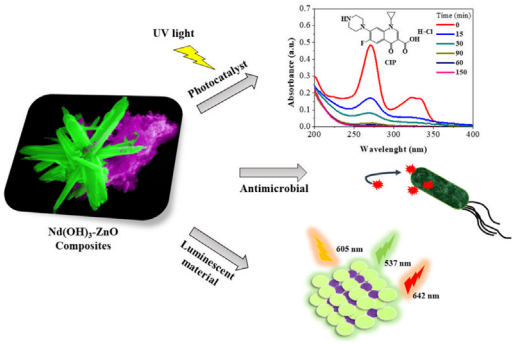

ARTICLE INFO

Keywords:
Photocatalyst
Antimicrobial agent
Hydroxide-oxide interaction
Box-Behnken design

ABSTRACT

$Nd(OH)_3$-ZnO composites were synthesized with three content of Neodymium (1, 3 and 5 wt%) and characterized in terms of their structural, morphological, vibrational, optical, surface, photocatalytic and antimicrobial properties. The $Nd(OH)_3$-ZnO composites are constituted by ZnO, which showed hexagonal structure, three-dimensional morphology analogous to an arrangement of flowers with hexagonal rods, and the $Nd(OH)_3$ in the hexagonal phase with irregularly spherical shape. The presence of the $Nd(OH)_3$ in the composites promoted some structural degree of disorder in the ZnO network as well as interstitial defects and oxygen vacancy, which improved photocatalytic and antimicrobial activity. From the Box-Behnken design and response surface methodology, it was determined that the $1Nd(OH)_3$-ZnO composite showed the highest photocatalytic activity, which was attributed to its higher crystallinity, smaller crystallite size and particle width, band gap energy close to ZnO and lower recombination rate compared to ZnO. $Nd(OH)_3$-ZnO composites showed higher antimicrobial activity against *E. coli* and *S. aureus* than ZnO pure, evidencing the synergistic effect between $Nd(OH)_3$ and ZnO in the composites. Therefore, this study highlights the synthesis of $Nd(OH)_3$-ZnO composites combining zinc oxide and neodymium hydroxide with excellent photocatalytic and antimicrobial activity, which can be used in different practical applications such as luminescent material, photocatalyst and antimicrobial agent.

* Corresponding author.
E-mail address: veronice.santana@unioeste.br (V. Slusarski-Santana).

https://doi.org/10.1016/j.cej.2019.123737
Received 2 August 2019; Received in revised form 22 November 2019; Accepted 5 December 2019
Available online 09 December 2019
1385-8947/

1. Introduction

ZnO is an n-type semiconductor which can be applied in several areas such as electrical and chemical devices, sensors, solar cells, lasers, heterogeneous photocatalysis and antimicrobial treatment [1–5] due to its physical and chemical properties. However, the properties of ZnO are influenced by the method of synthesis [4,6], doping [7,8] formation of the composite [9–11] and heterojunction [12,13]. This semiconductor can be prepared by various synthesis routes, such as precipitation [4,7,14], hydrothermal [6,14,15] and solochemical [4,16–19] methods. The precipitation is a simple and low cost technique for large-scale production [14]. The solochemical method is based on chemical reactions produced by adding a metal precursor to a heated alkaline solution under slow reagent mixture and controlled temperature. This method is considered simple, fast and inexpensive, since there is no need for additives and heat treatment at high temperatures for oxide production, avoiding parallel reactions, by-product formation and additional costs with complex equipment [4,16–19].

The combination of ZnO with other oxides, metals, non-metals and lanthanides can improve optical, photocatalytic and antimicrobial properties for reducing the electron-hole pair recombination rate, creating new active sites and enhancing the characteristics of different materials by generating a synergistic effect between them [16,20–23]. Although Neodymium, a rare earth metal from the lanthanum group, is often used in ZnO doping [17,18,24,25], it can also be employed in the form of a composite [23,26]. Azadi et al. [23] showed that ZnO-Ag-Nd nanocomposite has high photocatalytic activity in dye degradation, characterizing a cost-effective treatment method for low-concentration dye. Sin et al. [26] synthetized ZnO/Nd-doped BiOBr composite and attributed the high photocatalytic activity of this material to the effective separation of photogenerated electron-hole.

At present, literature lacks studies regarding the combination of oxides and hydroxides for application in photocatalysis and disinfection process. Hao et al. [27] synthesized ZnS/ZnO/$Ni(OH)_2$ bifunctional composites via one-step hydrothermal reaction, reaching high electrochemical performances and photocatalytic activity. Sanivarapu et al. [28] and Wang et al. [29] observed that $Nd(OH)_3$ and $La(OH)_3$ showed activity in photoelectrochemical water splitting and photocatalytic activity in degradation of the Congo red dye, respectively. The specific combination of zinc oxide and neodymium hydroxide in the form of composites has not been depicted in the literature.

This knowledge gap or insufficiency, coupled with the need for a complete study to understand how the hydroxide-oxide interaction influences the composites properties, especially those related to photocatalytic and antimicrobial activity, motivated the development of this research. Thus, the aim of this study was to synthesize and characterize composites constituted by $Nd(OH)_3$ and ZnO with different neodymium content (1, 3 and 5 wt%), called $Nd(OH)_3$-ZnO composites. The effect of the Nd content on the structural, morphological, vibrational, optical and surface properties was evaluated using the techniques of X-ray diffraction (XRD); scanning electron microscopy (SEM) and transmission electron microscopy (TEM); Fourier transform infrared spectroscopy (FT-IR) and Raman spectroscopy; UV–Vis diffuse reflectance spectroscopy (DRS) and photoluminescence (PL); and point of zero charge (pH_{PZC}), respectively. The photocatalytic activity of composites on the degradation of ciprofloxacin hydrochloride (CIP) under UV radiation was evaluated using 3-factor, 3-level Box-Behnken design and the response surface methodology (RSM). The disk diffusion method was used to evaluate the antimicrobial activity of the composites against *Escherichia coli* Gram-negative and *Staphylococcus aureus* Gram-positive bacteria. Therefore, the novelty of this study is the synthesis and characterization of composite combining ZnO and $Nd(OH)_3$ for possible application in heterogeneous photocatalysis, disinfection process and optic-electronic applications.

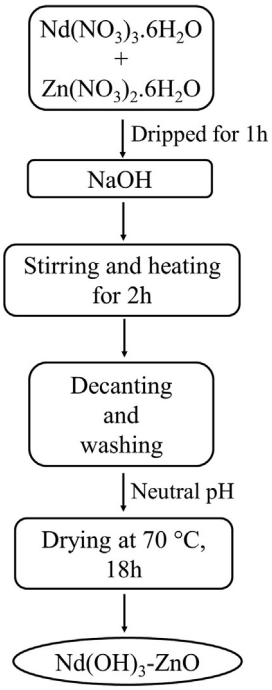

Fig. 1. The summarized procedure of preparing $Nd(OH)_3$-ZnO composites.

2. Materials and methods

2.1. Synthesis of $Nd(OH)_3$-ZnO composites

The methodology used in the synthesis of $Nd(OH)_3$-ZnO composites was a combination of the solochemical [16] and co-precipitation [30] methods with some adaptations. In a typical synthesis, 0.16, 0.50 and 0.84 g of $Nd(NO_3)_3{\cdot}6H_2O$ (Sigma Aldrich, 99.9%) corresponding to 1, 3 and 5 wt% Nd in relation to Zn respectively were mixed to 250 mL of 0.3 mol L^{-1} $Zn(NO_3)_2{\cdot}6H_2O$ (Synth, 99%) solution. Neodymium contents used in the synthesis of composites were defined from previous studies and literature. This solution was slowly dripped (for 1 h) in 250 mL of NaOH (NEON, 98.8%) solution (1 mol L^{-1}, pH 12) at 70 ± 3 °C under vigorous stirring (> 100 rpm). The dispersion was aged for 2 h with continuous stirring and heating. The precipitate was then separated by decantation, washed several times with water to neutral pH and dried at 70 ± 3 °C for 18 h. Pure ZnO was also synthesized according to this methodology. The procedure of preparing $Nd(OH)_3$-ZnO composite is briefly shown in Fig. 1.

2.2. Characterization of the composites

2.2.1. X-ray diffraction (XRD) and Rietveld refinemt

Crystal structure and phase of the composites were investigated by X-ray diffraction (XRD) using a D/Max-2500PC diffractometer (Rigaku, Japan) with Cu-Kα radiation source (λ = 1.5406 Å) in the 2θ range from 5° to 80°. The XRD patterns were compared with the ICSD database. The average crystallite size was determined from the ZnO (1 0 1) crystal plane using the Scherrer' formula with k equal to 0.9 [31]. The Rietveld refinement was performed by using the general structure analysis (GSAS) software using measured XDR patterns in the 2θ range from 10° to 110° with a scanning rate of 0.01°/min.

2.2.2. Scanning electron microscopy with energy dispersive X-ray spectroscopy (SEM-EDXS) and transmission electron microscopy (TEM)

The morphology and composition of the $Nd(OH)_3$-ZnO were characterized by scanning electron microscopy with energy dispersive X-ray spectroscopy (SEM-EDXS) and transmission electron microscopy

(TEM). SEM-EDXS analysis was carried out in a SEM microscope (FEI/Philips, Model: XL-30, Netherlands) equipped with an EDXS analyzer (Oxford, Model: Link ISIS 300, England). The sharpness of composites was observed by TEM using a FEI Tecnai F20 (Netherlands) microscope operating at 200 kV.

2.2.3. Fourier transform infrared (FT-IR) and Raman spectroscopy

The infrared vibrational bands of the $Nd(OH)_3$-ZnO were identified by Fourier transform infrared spectroscopy (FT-IR) in a spectrometer (Spectrum 100, Perkin Elmer). The spectra were obtained from KBr pellets containing 1 mg of composite and 100 mg of KBr in the region between 400 and 4000 cm^{-1}, using a resolution of 4 cm^{-1} and 8 accumulations.

The vibrational properties of the $Nd(OH)_3$-ZnO composites were also investigated by Raman spectroscopy in a FT-Raman spectrometer (RFS/100/S Bruker, Germany) equipped with laser of Nd-YAG (λ = 1064 nm) as excitation source and the laser power on the sample was 10 mW. For the region comprised between 40 and 1400 cm^{-1}, 30 scans with spectral resolution of 4 cm^{-1} were performed.

2.2.4. UV–Vis diffuse reflectance spectroscopy (DRS) and photoluminescence (PL)

The optical properties of the $Nd(OH)_3$-ZnO were characterized by UV–Vis diffuse reflectance spectroscopy (DRS) and the analysis was carried out in a spectrophotometer (Cary 5G Varian, United States), programmed in diffuse reflectance mode, in the wavelength range of 200–800 nm. The band gap energy (Eg) was determined from the Kubelka-Munk function: $F(R) = (1-R)^2/2R$, where R is the diffuse reflectance, and the Wood-Tauc plot: $[F(R) \times E]^{1/2}$ where E is the energy of absorbed light, by extrapolation of the straight line to the abscissa [32,33].

PL measurements were carried out at room temperature in a Monospec 27 monochromator (Thermal Jarrel Ash, United States) coupled to a R446 photomultiplier (Hamamatsu Photonics, Japan). As excitation source, a krypton-ionlaser (Coherent Innova 90 K; λ = 350.7 nm) with maximum output power of 200 mW was used. The analyses were carried out with 25 mg of $Nd(OH)_3$-ZnO.

2.2.5. Point of zero charge (pH_{PZC})

An adaptation of the Singh et al. [34] methodology was used to determinate pH_{PZC} of the $Nd(OH)_3$-ZnO. The pH of NaCl solution (50 mL, 0.01 mol L^{-1}) was adjusted from 2 to 12 with NaOH (0.01 and 5 mol L^{-1}) and HCl (0.01, 2.5 and 5% (v/v)) solutions in each batch. After adjustment, 0.1 g of composite was added in each solution. The dispersions remained for 24 h under stirring at 150 rpm, and then the final pH of the solutions were measured using a pHmeter. The pH_{PZC} corresponds to the condition in which the initial pH of the solution did not change in the presence of the composite ($pH_{final} = pH_{initial}$). This analysis was performed in triplicate and pH_{PCZ} was expressed as an average ± SD of these experiments.

2.2.6. Photocatalytic activity

The photocatalytic activity of the $Nd(OH)_3$-ZnO composites on the photocatalytic degradation of ciprofloxacin hydrochloride (CIP) was evaluated. The experimental tests were carried out in a batch photoreactor (25 cm of diameter) with water-cooled in outer jacket (T ≈ 25 °C) and magnetic agitation. Mercury vapor lamp (80 W, ECP) without the glass cover (emitting preferably ultraviolet radiation) was used as irradiation source, which was located at 15 cm from the surface of the solution to be treated. The intensity of the UV light was measured using an Apogee MU-200 radiometer and was determined to be 14 W cm^{-2}.

In the experimental assays, a certain amount (0.1–1.9 mg L^{-1}) of $Nd(OH)_3$-ZnO was dispersed in 350 mL of CIP solution (5–15 mg L^{-1}) and the dispersion was kept in the dark under stirring for 30 min. Then, the light radiation was switched on and the reaction was carried out for 150 min. After regular time intervals, samples were collected, centrifuged at 5000 rpm for 10 min and analyzed by UV–Vis spectrophotometry (UV-1800 Shimadzu) between 200 and 400 nm. The pH of the initial and final samples was also monitored. The efficiency of the CIP degradation was calculated according to the following equation: $E(\%) = 100 \times (C_{initial} - C_{final})/C_{initial}$; for the maximum absorption wavelength of CIP (276 nm). The kinetic data were adjusted by pseudo-first-order Langmuir-Hinshelwood mechanism in the exponential form $[C/C_{eq} = \exp(-k_{ap}t)]$ where: C is CIP concentration at time t; C_{eq} CIP concentration in the equilibrium (after 30 min in the dark); k_{ap} apparent first-order rate constant; and t irradiation time, using Origin software. The experiments were performed in triplicate and k_{ap} was expressed as an average ± SD of these results.

The 3-factor, 3-level Box-Behnken experimental design was employed to evaluated the influence of the independent variables (CIP concentration at 5, 10 and 15 mg L^{-1}, Nd content at 1, 3 and 5 wt%, and composite concentration at 0.1, 1 and 1.9 mg L^{-1}) on the apparent first-order rate constant (dependent variable). The experimental data were analyzed by nonlinear regression using a second-order polynomial model that considers main, quadratic and linear–linear interactive effects of the parameters. The analysis of variance (ANOVA) with a 95% confidence level ($p < 0.05$) was used to determine the adequacy of model in the Statistica software.

2.2.7. Antimicrobial activity

The antimicrobial activity of $Nd(OH)_3$-ZnO composites was investigated by the disk diffusion method according to NCCLS:M2-A8 methodology [35] against *Escherichia coli* Gram-negative (*E. coli*, ATCC 25922) and *Staphylococcus aureus* Gram-positive (*S. aureus*, ATCC 6538) bacteria. In this method, each microorganism (approximately 1×10^6 CFU mL^{-1}) was inoculated separately on sterile Petri-plates (60x15 cm) containing Mueller Hinton agar broth. Filter paper discs (6 mm in diameter) were moistened with sterile water and 8 mg of each $Nd(OH)_3$-ZnO composite were deposited on these discs, which were then placed on the agar plates seeded with the microorganism. After 24 h of incubation at 36 ± 1 °C, the inhibitory action of $Nd(OH)_3$-ZnO composites on the growth of the *E. coli* and *S. aureus* bacteria was determined by measuring inhibition zone. Sterile distilled water was used as negative control and ciprofloxacin hydrochloride (5 μg 10 mL^{-1}) was used as positive control. The assays were performed in triplicate and the diameter of the inhibition zone was expressed as an average ± SD of these results.

To assess the solubility of the $Nd(OH)_3$-ZnO composites in sterile water (release of Zn^{+2} and Nd^{+3} ions), 1 g L^{-1} of each composite was placed in sterile water and kept under stirring at 25 ± 3 °C. After 24 h, a sample was collected, filtered through 0.45 μm syringe filters and analyzed by total reflection X-ray spectrometry (TXRF). A portable benchtop TXRF spectrometer (S2 PICOFOX, Bruker AXS Microanalysis GmbH) was used and sample preparation was performed according to the methodology presented by Espinoza-Quiñones et al. [36]. This test was performed in triplicate and the average value was used.

3. Results and discussion

3.1. XRD analysis

$Nd(OH)_3$-ZnO composites showed sharp and well-defined diffraction peaks as can be visualized in the XRD patterns (Fig. 2), indicating a good degree of structural symmetry at long-range distances [37]. Thus, the method used in the synthesis of composites was efficient to synthesize structured materials with good degree of purity and symmetry without the need for heat treatment at high temperatures and addition of additives/surfactants in a relatively short time. The pure ZnO present hexagonal crystalline structure, according to the JCPDS card no. 36-1451 identified in the Fig. 2.A. With an addition of Nd to form the composites, $Nd(OH)_3$ in the hexagonal phase was observed (JCPDS card

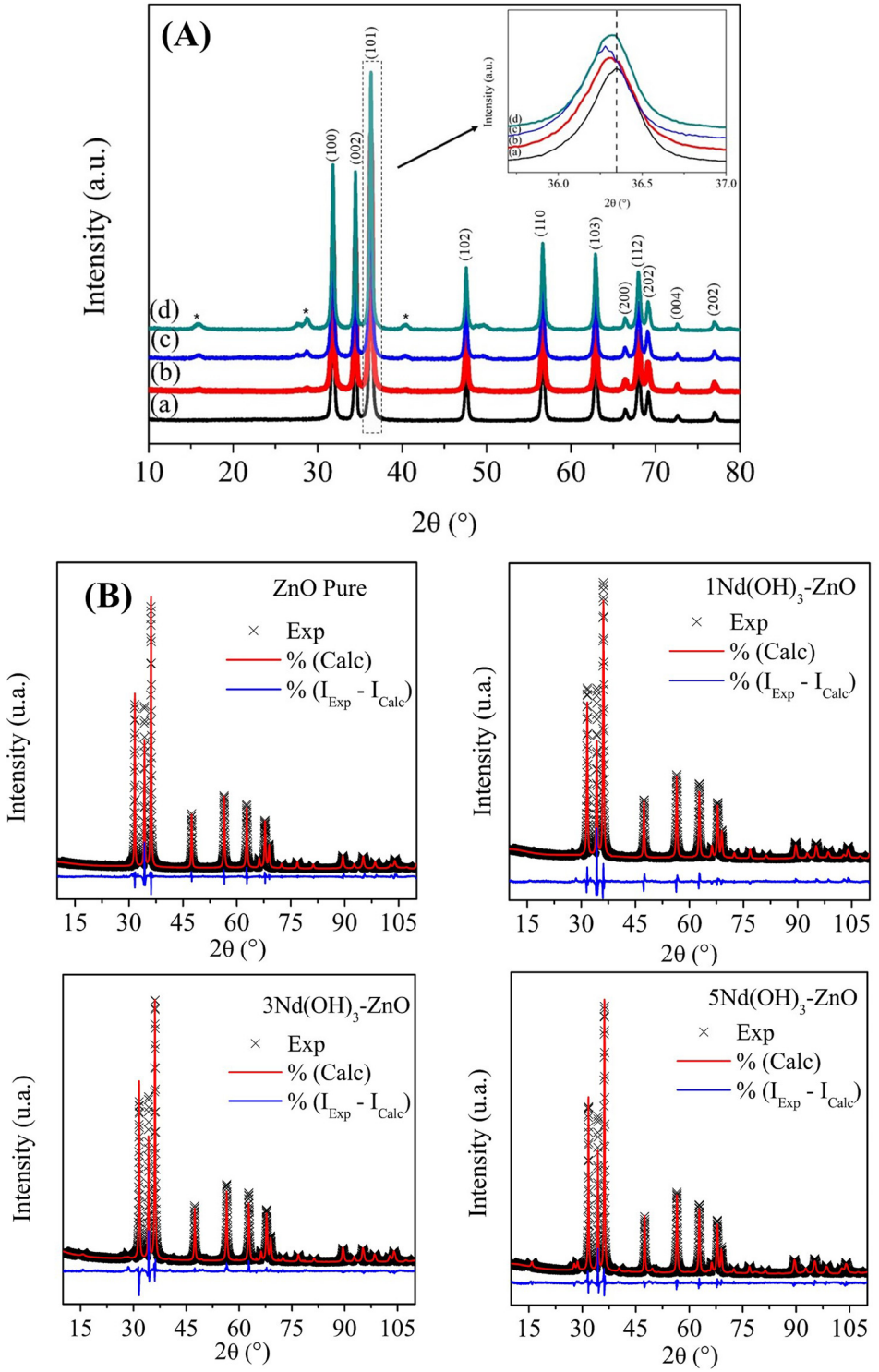

Fig. 2. XRD patterns of the (A) $Nd(OH)_3$-ZnO composites which (a) ZnO, (b) 1$Nd(OH)_3$-ZnO, (c) 3$Nd(OH)_3$-ZnO, (d) 5$Nd(OH)_3$-ZnO and (*) $Nd(OH)_3$; (B) Rietveld refinement plots.

no. 83-2035). The interaction of ZnO and $Nd(OH)_3$ promoted a slight shift in the diffraction angle of the three major peaks of the ZnO towards lower angles (insert in Fig. 2, Table 1). This behavior may be associated with the change in the crystallinity and morphology that provokes alteration in the tensile stress of the crystalline lattice (Table 1).

Fig. 2.B shows the Rietveld refinement plots of the XRD patterns for all $Nd(OH)_3$-ZnO samples. The results obtained by employing the Rietveld method are summarized and presented in Table 1. The fitting parameters (R_{bragg} and 2Θ) indicate good agreement between the XRD patterns calculated and observed for the as-prepared $Nd(OH)_3$-ZnO composites in this study. Moreover, the lattice parameters (a, b, c) and volume (V), which were estimated from the refinement, confirmed the hexagonal structure of the ZnO and $Nd(OH)_3$, and are in good agreement with the values reported in the literature. It can be observed that with the insertion of Nd and the consequent formation of the composites, there is a decrease of the lattice parameters, a, b and c, for the ZnO and $Nd(OH)_3$ and that they do not modify significantly with the

Table 1
Results obtained from Rietveld Refinements of $Nd(OH)_3$-ZnO composites and ZnO.

Materials	2θ	Crystallinity (%)	Crystal size (nm)[2]	ZnO				$Nd(OH)_3$				R_{Bragg} (%)	X^2 (%)	Wt fraction	
				a (Å)	b (Å)	c (Å)	V (cm^3)	a (Å)	b (Å)	c (Å)	V (cm^3)			ZnO	$Nd(OH)_3$
ZnO	36.33	83.8	32.33	3.26267	3.26267	5.22728	48.190	–	–	–	–	0,0807	5.890	–	–
1$Nd(OH)_3$-ZnO	36.34	83.6	32.31	3.25363	3.25363	5.21241	47.787	–	–	–	–	0,0598	6.383	1	–
3$Nd(OH)_3$-ZnO	36.32	82.4	32.19	3.25256	3.25256	5.21139	47.746	6.442	6.442	3.7454	134.59	0,0987	5.794	0.97701	0.02299
5$Nd(OH)_3$-ZnO	36.28	80.2	32.76	3.25149	3.25149	5.21005	47.702	6.4398	6.4398	3.7461	134.54	0,0802	7.721	0.97976	0.05024
Literature (I, II)[1]	–	–	–	3.2542	3.2542	5.201	47.7	6.437	6.437	3.747	134.46	–	–	–	–

[1] **I:** ICSD (ZnO): 181731; **II:** ICSD ($Nd(OH)_3$): 167,482.
[2] Calculated by the Scherrer equation with k = 0.9 to the (1 0 1) diffraction peak.

increase in the percentage of Nd. According to the literature [22,38,39], the composite formation can cause change in crystal growth orientation and distortion or expansion in the crystal lattice can be sensed.

The results show that a composite was formed by mixing $Nd(OH)_3$ and ZnO. Moreover, the real percentages of $Nd(OH)_3$ on the 1$Nd(OH)_3$-ZnO, 3$Nd(OH)_3$-ZnO, and 5$Nd(OH)_3$-ZnO are near to zero %, 2.3% and 5%, respectively. The differences in real and theoretical concentrations observed for the sample containing 1% Nd can be assigned to the low resolution of the software GSAS, used to perform the Rietveld refinement and also the small amount of $Nd(OH)_3$ on the composites.

3.2. SEM-EDXS and TEM analyses

Fig. 3 shows the SEM and TEM image, particle size distribution and EDSX spectrum of the $Nd(OH)_3$-ZnO composites. Observing the SEM and TEM image of the 1$Nd(OH)_3$-ZnO (Fig. 3.A, D), 3$Nd(OH)_3$-ZnO (Fig. 3.E, H) and 5$Nd(OH)_3$-ZnO (Fig. 3.I, L), respectively, two types of morphology can be evidenced. A three-dimensional morphology analogous to an arrangement of flowers with hexagonal microrods (c-axis growth) with an extremity of six-fold pyramidal geometry piled up closely emerging from a center, which was attributed to ZnO and can be well visualized in Fig. 3.I. This result is consistent with the literature [6,40,41]. The other structure related to $Nd(OH)_3$ presents irregularly spherical shape and as the Nd content increased, the formation of more agglomerates was observed. This result differs from those presented in the literature [15,42–44], which showed that $Nd(OH)_3$ particles synthesized by hydrothermal route generally present microrod or nanorod-like morphology. Thus, the influence of the synthesis method on the morphology of the particles is evident.

According to the micrographs and size distribution graphs (Fig. 3. B, F and J), three different situations were observed for the size of the composites in this study. In the 1$Nd(OH)_3$-ZnO sample the particles are mostly nanometric, with an average size in the range of 20–100 nm, which corresponds to approximately 80% of the total number of counts. For the 3$Nd(OH)_3$-ZnO sample, the nanometric particles correspond to 65% of the total, with sizes ranging from 20 to 240 nm. In the 5Nd $(OH)_3$-ZnO composite an average size between 100 and 120 nm was observed, of the total, only 35% of the particles are considered nanometric. By analyzing these results, it can be stated that the increase of $Nd(OH)_3$ content promoted an increase in particle size, which consequently altered flower formation by nanorod coupling. This increase in particle size correlates with the reduction in crystallinity as identified by XRD (Fig. 2 and Table 1). Although the morphology of ZnO in the composites was similar to those observed by Avci et al. [6], Chen et al. [40] and Byzynski et al. [41] that obtained 3D flowerlike ZnO microstructures with average size of 4–5 μm, 2–3 μm and 1.2–1.7 μm respectively, the $Nd(OH)_3$-ZnO composites presented much smaller average size (0.2–0.3 μm).

EDXS analysis (Fig. 3.C, G, K) carried out on the composites revealed the presence of Zn, O and Nd in the samples and although this analysis is semi-quantitative, the Nd content estimated was 0.29, 3.08 and 4.05% to 1$Nd(OH)_3$-ZnO, 3$Nd(OH)_3$-ZnO and 5$Nd(OH)_3$-ZnO, respectively. These values are close to those obtained by refinement Rietveld. The difference between real and theoretical content is due to the irregular dispersion of $Nd(OH)_3$ in the composite, as can be seen in Fig. 3.D, H, L. The result for 3$Nd(OH)_3$-ZnO can also be attributed to the lower percentage of oxygen in the material caused by the release of oxygen bonds with their cationic atom [45].

3.3. FT-IR and Raman analyses

The FT-IR and Raman spectra of the $Nd(OH)_3$-ZnO composites can be visualized in the Fig. 4. The $Nd(OH)_3$-ZnO samples presented a band at 487 cm^{-1}, which is attributed to formation of Zn-O bond, bands at 407 and 680 cm^{-1} referring to the vibration of the Nd-O bond and the sharp peak at 3608 cm^{-1} representing the OH of $Nd(OH)_3$ (Fig. 4.A). The increase in the Nd content made the last three bands more intense. These results are consistent with the literature [46,47]. All samples showed a broad band between 3434 and 3448 cm^{-1} and the band at 1634 cm^{-1}, which are attributed to the O-H stretching of adsorbed water and water deformation (H-O-H), respectively [46,48]. It was also possible to verify the bands at 882, 1385 and 1496 cm^{-1} coming from the precursor (nitrate) used in the composites synthesis. The symmetrical vibration of the NO bond of the NO_2 group is observed at 1385 cm^{-1}, whereas the bands at 882 and 1496 cm^{-1} are referential to the stretching of the π bonds of the N-O linkage and to the asymmetric vibration of the NO bond of the NO_2 group, respectively [49,50]. The bands at 882 and 1496 cm^{-1} were more pronounced in the composites than in the ZnO, while the band at 1385 cm^{-1} was higher for ZnO.

ZnO is a semiconductor with wurtzite crystal structure, with space group C_{6v}^4, and two formula units per primitive cell, where all atoms occupy C_{3v} sites. The Raman active zone-center optical phonons predicted by the group theory are $A_1 + 2E_2 + E_1$. The polar phonons, symmetry A_1 and E_1, exhibit different frequencies for the transverse-optical (TO) and longitudinal-optical (LO) phonons, whilst symmetry E_2, nonpolar phonon, displays two frequencies, one related to oxygen atoms, E_2 (high), and the other related with Zn sub-lattice, E_2 (low). Nd $(OH)_3$-ZnO composites were found to have Raman spectra at room temperature (Fig. 4.B) similar to that of pure ZnO. The narrow strong band at 433.04 cm^{-1} refer to the E_{2H} Raman-active phonon mode. The bands at 327.66 and 374.40 cm^{-1} can be attributed to the $3E_{2H}$-E_{2L} and A_1 (TO) phonon modes respectively, the latter mode indicates the presence of some structural degree of disorder in the ZnO network at short range. The bands at 531.61 and 580.05 cm^{-1} are contributions of the E_1(LO) and A_1(LO) phonon modes, respectively, which are associated to the interstitial defects and oxygen vacancy in the ZnO lattice [51,52]. The band at 1047.88 cm^{-1} is attributed to multiple phonon scattering processes – A_1(TO) + E_1(TO) + E_{2L} second order phonon

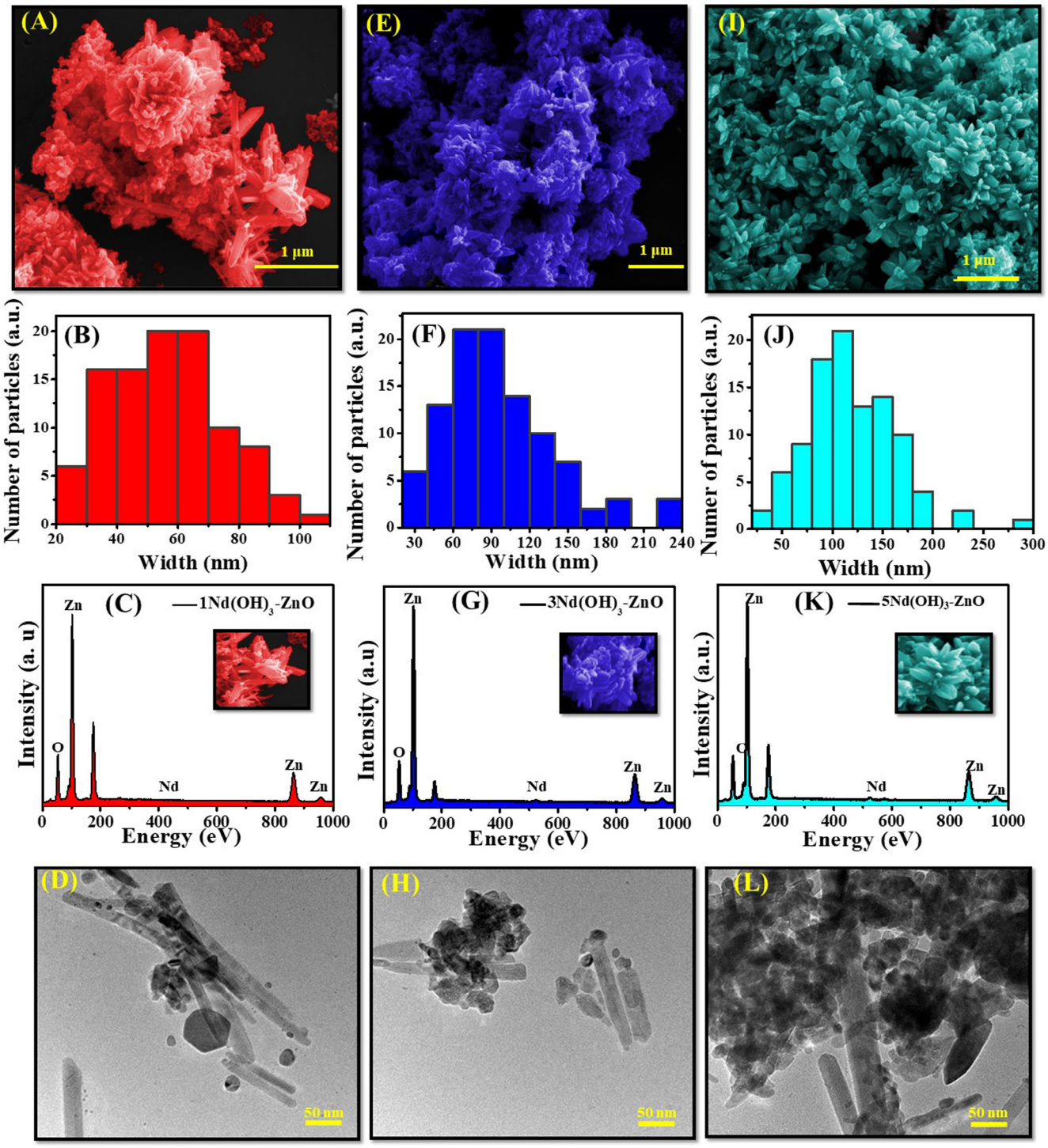

Fig. 3. SEM image, particle size distribution of each composite, EDSX spectrum and TEM image of the (A, B, C, D) 1Nd(OH)$_3$-ZnO, (E, F, G, H) 3Nd(OH)$_3$-ZnO and (I, J, K, L) 5Nd(OH)$_3$-ZnO, respectively. Inset part in figure was the magnification of SEM image.

mode [53] – disappeared in the Nd(OH)$_3$-ZnO samples due to the hydroxide-oxide interaction that promoted the lattice structure disorder. According to the literature [15,28], Nd(OH)$_3$ shows the A_{1g}, E_{2g} and E_{1g} Raman-active vibrations around 216–294, 351–365 and 472–544 cm^{-1}, respectively. These modes are not observed on the spectral due to the low amount of Nd(OH)$_3$ or the overlap with the ZnO modes.

3.4. DRS and PL analyses

The UV–Vis diffuse reflectance spectra of the Nd(OH)$_3$-ZnO composites and pure ZnO (Fig. 5) showed three and two distinct regions respectively. A weak absorption region up to 360 nm, an absorption edge region between 360 and 415 nm corresponding to the band-band transition with energy between 3.0 and 3.3 eV, and a strong absorption region located from 415 to 800 nm, due to the presence of rare earth Nd (the pure ZnO does not show absorption in this region). The band gap energy of the Nd(OH)$_3$-ZnO composites is close to the value obtained by

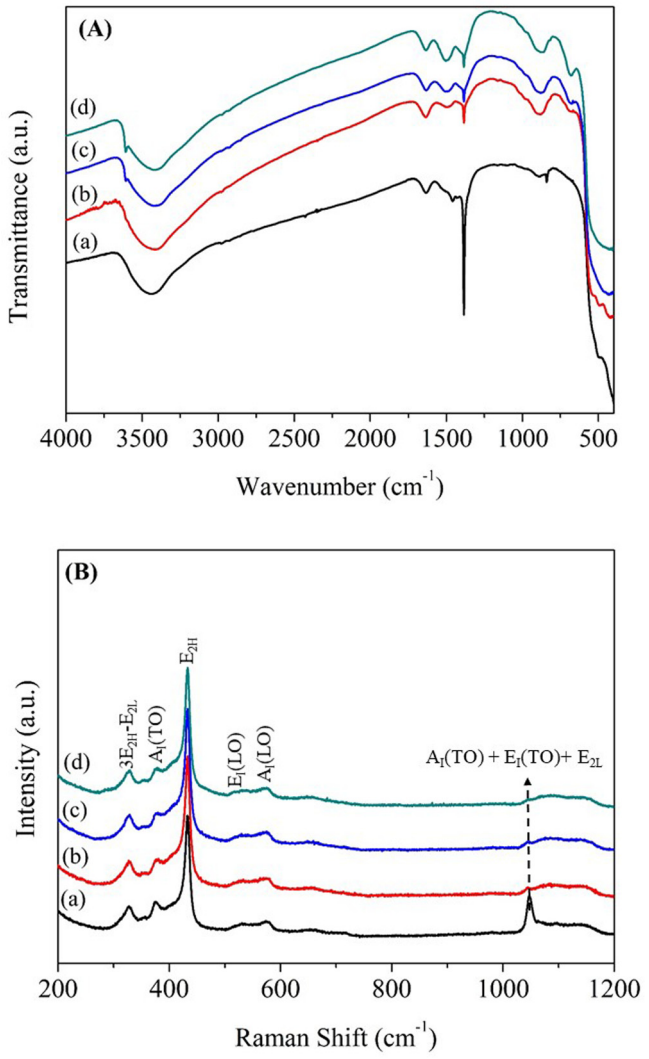

Fig. 4. Spectra of (A) FT-IR and (B) Raman of the $Nd(OH)_3$-ZnO composites, which (a) ZnO, (b) $1Nd(OH)_3$-ZnO, (c) $3Nd(OH)_3$-ZnO and (d) $5Nd(OH)_3$-ZnO.

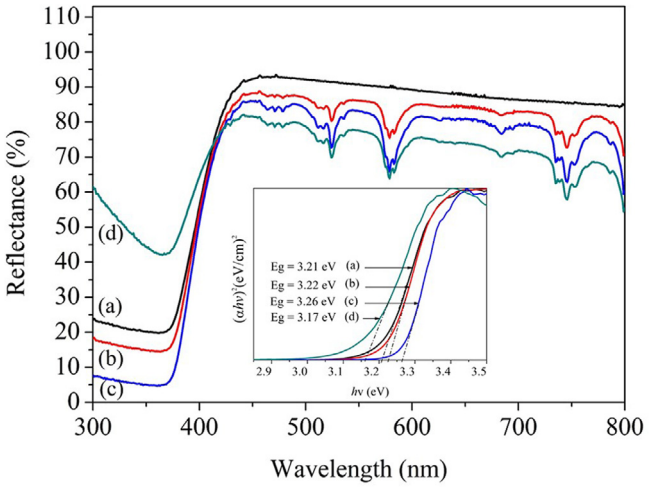

Fig. 5. UV–Vis DRS absorption spectra with insertion of band gap energy of the $Nd(OH)_3$-ZnO composites which (a) ZnO, (b) $1Nd(OH)_3$-ZnO, (c) $3Nd(OH)_3$-ZnO and (d) $5Nd(OH)_3$-ZnO.

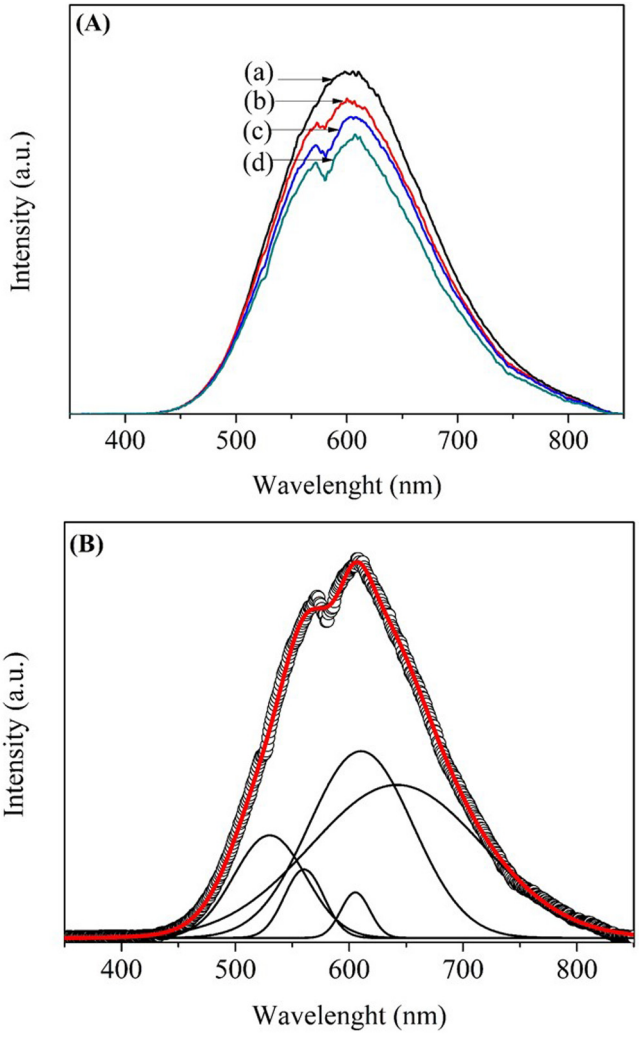

Fig. 6. Emission spectra of the (A) $Nd(OH)_3$-ZnO composites which (a) ZnO, (b) $1Nd(OH)_3$-ZnO, (c) $3Nd(OH)_3$-ZnO and (d) $5Nd(OH)_3$-ZnO at room temperature; (B) Gaussian de-composed PL spectrum of the $5Nd(OH)_3$-ZnO.

Sin et al. [26] for ZnO/Nd-BiOBr composite (3.11 eV).

In the region above 400 nm, there were only bands (525, 575–583 and 735–753 nm) that correspond to the intra-configurational ($4f^3$) transition of Nd^{+3} starting from the $^4I_{9/2}$ ground state configuration to $^2K_{13/2}$ + $^4G_{7/2}$, $^2G_{7/2}$ + $^4G_{5/2}$ and $^4S_{3/2}$ + $^4F_{7/2}$ + $^2H_{9/2}$ lowest-energy multiplet manifolds, respectively [46,54]. The greater the amount of Nd the higher the bands intensity in the visible region, but the format remained. According to Dhamale et al. [46], this similarity of the spectra occurs because the f-orbital electrons of Nd^{+3} that participate in the transition are not affected by the neighboring atoms. This result is similar to those obtained by Sin et al. [55] and Chandran et al. [56] and confirms that $Nd(OH)_3$-ZnO composites also absorb visible light and can be promising photocatalysts for application in visible light photocatalysis.

The PL emission spectra of the ZnO and $Nd(OH)_3$-ZnO composites are shown in the Fig. 6. In general, ZnO presented the highest signal of PL emission and the increase on the Nd content reduced the PL intensity of the composites (Fig. 6.A). The high PL intensity indicates that the synthesis method generated materials with an optimum structural order degree. The reduction of the PL signal in the $Nd(OH)_3$-ZnO indicates that there is a greater number of free electron-hole pairs due to the inhibition of the recombination rate in the composites. Neodymium caused this inhibition due to the generation of more crystal defects, such as oxygen and zinc vacancies and interstitial oxygen [38,52] as

also evidenced in Raman analysis (Fig. 4.B), where the band at 531.61 and 580.05 cm^{-1} are associated to the interstitial defects and oxygen vacancies. Moreover, this result is in agreement with the literature [24].

Based on the Gaussian de-composed PL spectra, ZnO showed three peaks centered at 537 nm (green region), 597 nm (yellow region) and 662 nm (red region), which can be attributed to intrinsic defects such as interstitial oxygen [53], doubly positively charged oxygen vacancies (V_O^{++}) [30] or interstitial oxygen vacancies [24]. As $Nd(OH)_3$-ZnO composites had similar Gaussian de-composed PL spectra, only 5Nd $(OH)_3$-ZnO spectrum was shown in the Fig. 6.B. The $Nd(OH)_3$-ZnO composites spectra showed five peaks centered around 530, 560, 605, 610 and 642 nm that correspond to two green emissions, two orange emissions and one red emission, respectively. It is known that these emissions in the visible region are attributed to impurities such as intrinsic defects such as interstitial oxygen [53], singly charged oxygen vacancies (V_O^{+}) [30], zinc vacancies [24] deep level defects [57] and radiative recombination between delocalized electron and hole in the oxygen interstitials and oxygen and zinc anti-sites [53].

The red emission presented the highest shift as a function of the Nd content (756, 661 and 642 nm for 1$Nd(OH)_3$-ZnO, 3$Nd(OH)_3$-ZnO and 5$Nd(OH)_3$-ZnO, respectively). This red shift may occur due to lattice distortion, deep defect points and charge carriers that usually occurs in oxygen-rich materials [24,57], as well as crystal defects generated during the synthesis [10,58]. Other factors may be related to changes in PL emission spectra, such as morphology and particle size difference and interaction between ZnO and $Nd(OH)_3$ as evident by the SEM and TEM image (Fig. 3).

3.5. Point of zero charge (pH_{PZC})

The point of zero charge represents the condition in which the electrical charge density on material surface is zero. When the solution pH is lower than pH_{PZC}, the catalyst surface is positively charged and the electrostatic forces favor the anions adsorption. Cation adsorption is favored when the solution pH is higher than pH_{PZC} because in this condition, the surface of the catalyst is negatively charged [34,59]. The increase of the Nd content did not affect the pH_{PZC} of the $Nd(OH)_3$-ZnO composites, only the interaction between $Nd(OH)_3$ and ZnO shifted the pH_{PZC} to higher pH values (8.3 ± 0.3) in relation to pure ZnO (7.5 ± 0.3), indicating that the $Nd(OH)_3$-ZnO samples will be positively charged in a higher pH range. The difference of pH_{PZC} between composites and ZnO may be related to differences in coordination of $-O^-$ and -OH sites to cations, higher amount of surface adsorbed hydroxyls and oxygen vacancies [60] as observed in the FTIR (Fig. 4.A) and PL (Fig. 6) analyses.

3.6. Photocatalytic activity

The photocatalytic activity of the $Nd(OH)_3$-ZnO composites was evaluated on the degradation of the ciprofloxacin hydrochloride (CIP) and from the degradation profile, the apparent first-order rate constant (k_{ap}) and degradation efficiency of CIP (E%) were determined for each of the assays (Table 2). The composites showed high photocatalytic activity with degradation efficiency greater than 80% and k_{ap} between 0.012 ± 0.001 and 0.044 ± 0.001 min^{-1}, depending on the operational condition used.

From the Box-Behnken experimental design, the linear-linear influence of parameters like catalyst concentration (0.1, 1 and 1.9 mg L^{-1}), Nd content (1, 3 and 5%) and CIP concentration (5, 10 and 15 mg L^{-1}) on the CIP photocatalytic degradation was evaluated and the apparent first-order rate constant can be predicted using equation (1)

Table 2
Results of photocatalytic tests according to Box-Behnken design.

[CAT] g L^{-1}	%Nd	[CIP] mg L^{-1}	E[1] (%)	k_{ap}[2] (min^{-1})	R^2	k_{pred}[3] (min^{-1})
0.1	3	5	89	0.018 ± 0.001	0.968	0.018 ± 0.001
1.9	3	5	99	0.041 ± 0.002	0.987	0.042 ± 0.002
0.1	3	15	82	0.010 ± 0.001	0.979	0.010 ± 0.001
1.9	3	15	94	0.019 ± 0.001	0.986	0.020 ± 0.001
0.1	1	10	94	0.023 ± 0.001	0.977	0.023 ± 0.001
1.9	1	10	98	0.041 ± 0.002	0.989	0.040 ± 0.002
0.1	5	10	85	0.012 ± 0.001	0.964	0.012 ± 0.001
1.9	5	10	98	0.029 ± 0.001	0.995	0.029 ± 0.001
1.0	1	5	99	0.044 ± 0.001	0.995	0.044 ± 0.001
1.0	1	15	91	0.017 ± 0.001	0.994	0.018 ± 0.001
1.0	5	5	97	0.024 ± 0.001	0.997	0.023 ± 0.001
1.0	5	15	93	0.018 ± 0.001	0.993	0.018 ± 0.001
1.0	3	10	98	0.028 ± 0.001	0.997	0.029 ± 0.001
1.0	3	10	99	0.028 ± 0.001	0.995	0.029 ± 0.001
1.0	3	10	99	0.030 ± 0.001	0.997	0.029 ± 0.001

[1] E = Efficiency of degradation.
[2] k_{ap} = Apparent first-order rate constant determined experimentally (average value ± SD).
[3] k_{pred} = Apparent first-order rate constant calculated by the model equation (average value ± SD).

$$k_{ap} = 0.032960 + 0.02483\ x\ [Cat] + 0.000535\ x\ [CIP] - 0.003870\ x\ [Cat]^2 - 0.000145\ x\ [CIP]^2 - 0.007875\ x\ [\%Nd] - 0.000778\ x\ [Cat]\ x\ [CIP] + 0.000525\ x\ [CIP]\ x\ [\%Nd] \quad (1)$$

The terms with positive and negative signals in the Equation (1) favor and disfavor the reaction rate, respectively, and the catalyst concentration was the most influential term. The values of k_{pred} (Table 2) were very close to the k_{ap} determined experimentally, indicating that the model predicts well the experimental data.

The adequacy of the model was evaluated by analysis of variance (ANOVA) and the results are found in Table 3. As the R^2 and Adj-R^2 values were high and close to 1 (0.994 and 0.988, respectively) and the difference between them was less than 20%, this indicates significance of the model [61,62]. The value of Fisher's F test (F_{model} = 163.1317) with a very low probability value (p_{model} = 0.000014) was higher than the critical F value ($F_{(0.05,7,2)}$ = 19.35), indicating the adequacy of the quadratic model used to represent the data. As the value of lack of fit was non-significant ($p > 0.05$), the quadratic model was valid [62], but it is far from the maximum point (optimal condition). This is not a problem in this study because no optimization was carried out, only the evaluation of the effect of each parameter on the apparent first-order rate constant, proving that the $Nd(OH)_3$-ZnO composites have photocatalytic activity.

The parameters effects on the apparent first-order rate constant can be understood from response surface methodology (RSM). The 3D plots in the Fig. 7 were constructed based on the quadratic model for CIP

Table 3
Analysis of variance (ANOVA) for the CIP degradation using $Nd(OH)_3$-ZnO composites.

Source	Sum of squares	df	Mean squares	F-value	p-value
Model	0.001523	7	0.000217	163.1317	0.000014
(1) [Cat] (L + Q)	0.000598	2	0.000299	224.1078	0.004442
(2) [CIP] (L + Q)	0.000545	2	0.000273	204.4471	0.004867
(3) %Nd (L)	0.000221	1	0.000221	165.3750	0.005993
1*2	0.000049	1	0.000049	36.7500	0.026148
2*3	0.000110	1	0.000110	82.6875	0.011879
Residual	0.000009	7	0.000001		
Lack of Fit	0.000006	5	0.000001	0.9212	0.594074
Pure Error	0.000003	2	0.000001		
Total SS	0.001526	14			

R^2 = 0.994; Adj-R^2 = 0.988; $F_{(0.05,7,2)}$ = 19.35.

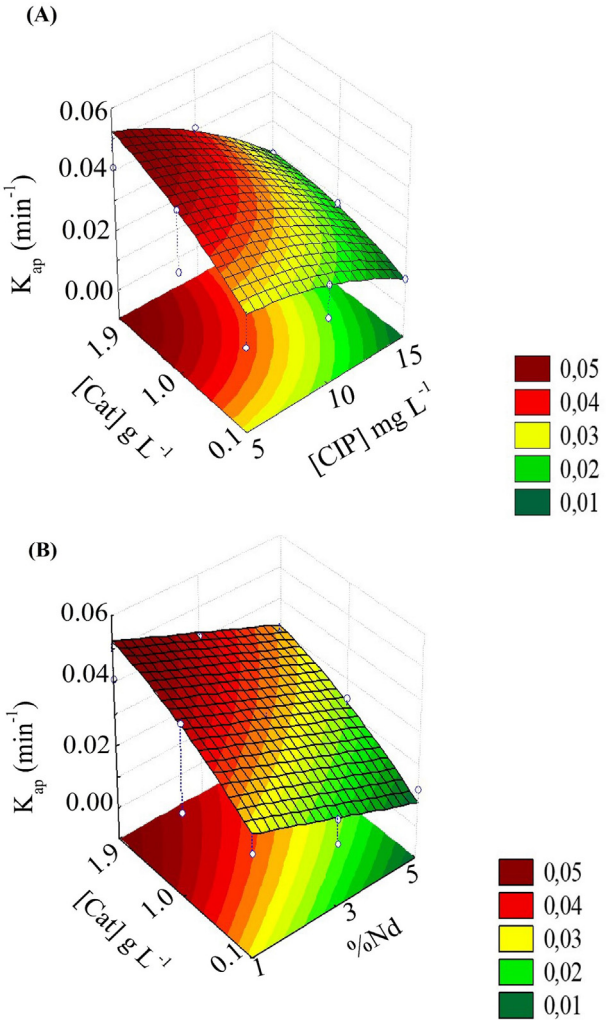

Fig. 7. 3D plots for (A) CIP concentration as a function of the catalyst concentration to 1Nd$(OH)_3$-ZnO and (B) %Nd as a function of the catalyst concentration to 5 mg L^{-1} of CIP.

concentration as a function of the catalyst concentration to 1Nd$(OH)_3$-ZnO and %Nd as a function of the catalyst concentration to 5 mg L^{-1} of CIP. As expected, according to the literature [63,64], the CIP concentration had a negative effect on the apparent first-order rate constant (k_{ap}), and it was faster to degrade diluted solutions (Fig. 7.A). The near circular contour of the lines in this plot suggested an interactive influence between CIP and catalyst concentration on the k_{ap}. The increase in the catalyst concentration favored k_{ap} (Fig. 7.A and B), which is related to the increase in the number of active sites on the catalyst surface [63]. However, the optimum range is around 1.9 g L^{-1} because concentration much higher than this can promote reduction of k_{ap} due to the reduction of light penetration caused by excess catalyst particles [64].

The Nd content showed little influence with higher k_{ap} values for 1Nd$(OH)_3$-ZnO composite (Fig. 7.B). Almost parallel contour lines along the %Nd coordinate suggested no significant interaction between the %Nd and catalyst concentration on the k_{ap}. The higher efficiency of 1Nd$(OH)_3$-ZnO can be attributed to its characteristics: higher crystallinity (Table 2), smaller crystallite size and particle width (Figs. 2 and 3), band gap energy close to ZnO (Fig. 5) and lower recombination rate compared to ZnO (Fig. 6). Thus, to obtain a rapid degradation of CIP it is necessary to work in low concentrations of CIP and Nd content and in high concentrations of catalyst, establishing within the studied range: 5 mg L^{-1} of CIP, 1Nd$(OH)_3$-ZnO and 1.45–1.9 g L^{-1} of catalyst.

As it was verified that the lowest Nd content promoted the best results, tests with pure ZnO were performed to evaluate the synergistic effect between Nd$(OH)_3$ and ZnO in the composite. For 5 mg L^{-1} of CIP and 1.0, 1.45 and 1.9 g L^{-1} of catalyst, ZnO showed k_{ap} of 0.024 ± 0.001, 0.041 ± 0.001 and 0.048 ± 0.002 min^{-1}, respectively. These values are lower than those presented by 1Nd$(OH)_3$-ZnO (0.044 ± 0.001, 0.051 ± 0.001 and 0.053 ± 0.002 min^{-1}), indicating that the Nd$(OH)_3$-ZnO composites have higher photocatalytic activity than pure ZnO. This confirms the synergistic effect between Nd$(OH)_3$ and ZnO due to its higher pH_{PZC} value and the inhibition of the recombination rate and consequent increase in the number of free electron-hole pair in the composite (Fig. 6). The k_{ap} value for 1Nd$(OH)_3$-ZnO composite is higher than those observed by Azadi et al. [23] and Sin et al. [26] when using ZnO-Ag-Nd nanocomposite and ZnO/Nd-BiOBr composite in the phenol (0.0332 min^{-1}) and Acid red 18 dye (0.0363 min^{-1}) degradation.

These results of Nd$(OH)_3$-ZnO composites are associated to reactive species formed during the photodegradation that can be used by the reaction mechanism. Pure ZnO is an n-type semiconductor with a certain density of oxygen vacancies. These vacancies produce holes that interact with water molecules resulting in hydroxyl radicals ($^{\cdot}OH$), and protons. On the other hand, due to electroneutrality, the semiconductor produces electrons that interact with oxygen, which in turn neutralize interacting with the proton, giving rise to the peroxide radical ($^{\cdot}O_2H$). With the formation of the Nd$(OH)_3$-ZnO composite, the presence of Nd$(OH)_3$ in the composite causes an increase in oxygen vacancies (V_O^+) density and consequently zinc vacancy density, favoring the formation of more hydroxyl radicals ($V_O^+ + h^+ \rightarrow V_O^{++} + OH^- \rightarrow V_O^+ + {}^{\cdot}OH$). In addition, another step involved in the degradation mechanism may be associated with greater efficiency in electron-hole charge separation, which slows down recombination processes, allowing active species formed in solution to remain free longer. The contributions of both steps favor the increase of photocatalytic activity of Nd$(OH)_3$-ZnO composites. These two radicals oxidize organic materials in water and carbon dioxide [65,66]. A simplified illustration of the possible mechanism of CIP photocatalytic degradation can be visualized in the Fig. 8 (mechanism A).

3.7. Antimicrobial activity

The antimicrobial activity of the Nd$(OH)_3$-ZnO composites was investigated against *Escherichia coli* Gram-negative and *Staphylococcus aureus* Gram-positive bacteria. The diameter of the inhibition zone that represents the inhibitory action on the growth of the bacteria was used. The Nd$(OH)_3$-ZnO composites have antimicrobial activity against both microorganisms as can be seen from Table 4; however, *E. coli* was more resistant to composites than *S. aureus* due to the structure and composition of cell wall. While *E. coli* has an external lipopolysaccharide layer that protects the peptidoglycan layer, *S. aureus* has a simpler structure, only one outer peptidoglycan layer, which facilitates the penetration of external molecules that will cause intracellular oxidative stress, damage and destruction of the cell cytoplasm, accelerating the death process of the microorganism [67,68]. Zanet et al. [69] also observed higher inhibition zone for *S. aureus* (0.8 ± 0.01 cm) compared to *E. coli* (0.7 ± 0.01 cm) using 1 g L^{-1} of ZnO nanoparticles.

It was also observed in Table 4 that the antimicrobial activity of the Nd$(OH)_3$-ZnO composites was higher than that of ZnO, evidencing a synergistic effect between Nd$(OH)_3$ and ZnO in these materials, and there was a reduction in the inhibition zone with the increase of Nd content. Among the evaluated materials, 1Nd$(OH)_3$-ZnO composite presented the highest antimicrobial activity (1.5 ± 0.1 cm for *E. coli* and 1.8 ± 0.1 cm for *S. aureus*) due to its particle size, mostly nanometric with an average size in the range of 20–100 nm (Fig. 3). The neodymium compounds, as with all rare earth metals, are of low to moderate toxicity for humans but toxic against microorganisms.

The inhibitory action of Nd$(OH)_3$-ZnO composites on the

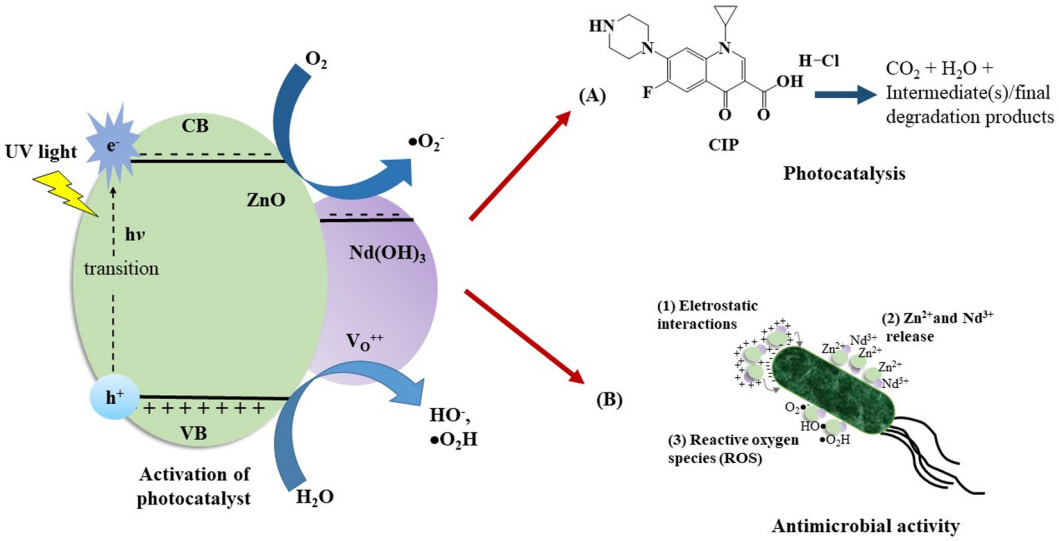

Fig. 8. Simplified illustration of the possible mechanism of (A) CIP photocatalytic degradation and (B) disinfection.

Table 4
Zone of inhibition (average value ± SD, in cm) of $Nd(OH)_3$-ZnO composites, ZnO and positive control against *Escherichia coli* and *Staphylococcus aureus*.

Material	Zone of inhibition (average value ± SD, in cm)	
	E. coli	*S. aureus*
$1Nd(OH)_3$-ZnO	1.5 ± 0.1	1.8 ± 0.1
$3Nd(OH)_3$-ZnO	1.3 ± 0.1	1.6 ± 0.1
$5Nd(OH)_3$-ZnO	1.2 ± 0.1	1.5 ± 0.1
ZnO	1.1 ± 0.1	1.3 ± 0.1
Ciprofloxacin	2.3 ± 0.1	2.8 ± 0.1

antibacterial growth can be attributed to three mechanisms [70–72], in this order of contribution: (1) Direct interaction between $Nd(OH)_3$-ZnO particles and microorganism by attachment of particles to the cell membrane due to electrostatic interaction that internalize and damage the microbial cell. This mechanism is favored by the smaller particle size (20–100 nm) of the $1Nd(OH)_3$-ZnO composite, as shown in Fig. 3, mostly nanometric (80%), since the smaller the particle size the greater the antimicrobial activity [73,74] and also by its surface charge that promotes electrostatic interaction. (2) Release of Zn^{+2} and Nd^{+3} ions that can easily penetrate into the cell wall and leads to microbial death. TXRF analysis results showed that the solubilization of the $Nd(OH)_3$-ZnO composites is low in sterile water with 0.22–0.23% Zn^{+2} and 0.10–0.15% Nd^{+3} leaching. Gilbertson et al. [75] and Baek et al. [76] showed that the toxicity of CuO and ZnO particles against Gram-positive and Gram-negative bacteria was much higher than the toxicity of Cu^{+2} and Zn^{+2} ions, respectively. Thus, antimicrobial activity of Nd $(OH)_3$-ZnO composites against *E. coli* and *S. aureus* may be due to particle toxicity rather than ions. (3) Attack of reactive oxygen species (ROS), causing damage to cell wall, leakage of minerals, protein and genetic material and consequent cell death. According to the literature [72,75], the particles demonstrate lower antimicrobial activity in the dark than in the presence of light, and as the antimicrobial assays in this study were performed in the absence of light, it is believed that the contribution of ROS on the antimicrobial activity of $Nd(OH)_3$-ZnO composites is smaller compared to other mechanisms. A simplified illustration of this disinfection mechanism can be visualized in the Fig. 8 (mechanism B).

4. Conclusion

$Nd(OH)_3$-ZnO composites synthesized in this study are constituted by two phases, hexagonal wurtzite crystalline structure of the ZnO and hexagonal crystalline structure of the $Nd(OH)_3$, and have vibrational bands characteristic of the Zn-O, Nd-O and Nd-OH bonds, photoluminescence properties, band gap energy between 3.17 and 3.26 and pH_{PZC} of 8.3 ± 0.3. $1Nd(OH)_3$-ZnO composite has particles mostly nanometric with an average size in the range of 20–100 nm and due to this, a greater photocatalytic and antimicrobial activity was observed with this material, confirming the synergistic effect between $Nd(OH)_3$ and ZnO in the composites. The advantages of $Nd(OH)_3$-ZnO composites are easy preparation, no additives, no heat treatment and photoluminescence, photocatalytic and antimicrobial characteristics. Therefore, this study showed that it is possible to prepare structured materials combining neodymium hydroxide and zinc oxide with specific characteristics such as crystalline structure, photoluminescence and high photoactivity and antimicrobial activity. Thus, $Nd(OH)_3$-ZnO composites can be used as luminescent materials, photocatalyst and antibacterial agent.

Declaration of Competing Interest

The authors declare that they have no known competing financial interests or personal relationships that could have appeared to influence the work reported in this paper.

Acknowledgments

The authors are grateful for the support of the Brazilian research financing institution: Coordenação de Aperfeiçoamento de Pessoal de Nível Superior (CAPES) - Finance Code 001 and FAPESP CEPID CDMF 2016/05661-3.

References

[1] R. Chen, B. Ling, X.W. Sun, H.D. Sun, Room temperature excitonic whispering gallery mode lasing from high-quality hexagonal ZnO microdisks, Adv. Mater. 23 (2011) 2199–2204, https://doi.org/10.1002/adma.201100423.
[2] R. Saravanan, H. Shankar, T. Prakash, V. Narayanan, A. Stephen, ZnO/CdO composite nanorods for photocatalytic degradation of methylene blue under visible light, Mater. Chem. Phys. 125 (2011) 277–280, https://doi.org/10.1016/j.matchemphys.2010.09.030.
[3] Y. Wang, G. She, H. Xu, Y. Liu, L. Mu, W. Shi, Cu_2O nanoparticles sensitized ZnO nanorod arrays: electrochemical synthesis and photocatalytic properties, Mater. Lett. 67 (2012) 110–112, https://doi.org/10.1016/j.matlet.2011.09.046.
[4] P.M. Perillo, M.N. Atia, D.F. Rodríguez, Effect of the reaction conditions on the formation of the ZnO nanostructures, Phys. E Low-Dimensional Syst. Nanostructures 85 (2017) 185–192, https://doi.org/10.1016/j.physe.2016.08.029.

[5] S. Lam, J. Sin, A.Z. Abdullah, A.R. Mohamed, ZnO nanorods surface-decorated by WO_3 nanoparticles for photocatalytic degradation of endocrine disruptors under a compact fluorescent lamp, Ceram. Int. 39 (2013) 2343–2352, https://doi.org/10.1016/j.ceramint.2012.08.085.

[6] G.G. Avcı, C.Z. Koyuncu, Morphologically controlled synthesis of flower shaped ZnO crystals with hexagonal rods and thick petals by hydrothermal method, Mater. Lett. 110 (2013) 83–86, https://doi.org/10.1016/j.matlet.2013.07.089.

[7] M.G. Nair, M. Nirmala, K. Rekha, A. Anukaliani, Structural, optical, photo catalytic and antibacterial activity of ZnO and Co doped ZnO nanoparticles, Mater. Lett. 65 (2011) 1797–1800, https://doi.org/10.1016/j.matlet.2011.03.079.

[8] S. Chauhan, M. Kumar, S. Chhoker, S.C. Katyal, V.P.S. Awana, Structural, vibrational, optical and magnetic properties of sol-gel derived Nd doped ZnO nanoparticles, J. Mater. Sci. Mater. Electron. 24 (2013) 5102–5110, https://doi.org/10.1007/s10854-013-1530-6.

[9] M.R. Vaezi, Two-step solochemical synthesis of ZnO/TiO_2 nano-composite materials, J. Mater. Process. Technol. 205 (2008) 332–337, https://doi.org/10.1016/j.jmatprotec.2007.11.122.

[10] S.M. Lam, J.C. Sin, I. Satoshi, A.Z. Abdullah, A.R. Mohamed, Enhanced sunlight photocatalytic performance over Nb_2O_5/ZnO nanorod composites and the mechanism study, Appl. Catal. A Gen. 471 (2014) 126–135, https://doi.org/10.1016/j.apcata.2013.12.001.

[11] J.E. Casillas, F. Tzompantzi, S.G. Castellanos, G. Mendoza-Damián, R. Pérez-Hernández, A. López-Gaona, A. Barrera, Promotion effect of ZnO on the photocatalytic activity of coupled Al_2O_3 -Nd_2O_3 -ZnO composites prepared by the sol − gel method in the degradation of phenol, Appl. Catal. B Environ. 208 (2017) 161–170, https://doi.org/10.1016/j.apcatb.2017.02.030.

[12] S.Y. Tsai, M.H. Hon, Y.M. Lu, Fabrication of transparent p-NiO/n-ZnO heterojunction devices for ultraviolet photodetectors, Solid. State. Electron. 63 (2011) 37–41, https://doi.org/10.1016/j.sse.2011.04.019.

[13] R.R. Prabhu, A.C. Saritha, M.R. Shijeesh, M.K. Jayaraj, Fabrication of p-CuO/n-ZnO heterojunction diode via sol-gel spin coating technique, Mater. Sci. Eng. B Solid-State Mater. Adv. Technol. 220 (2017) 82–90, https://doi.org/10.1016/j.mseb.2017.03.008.

[14] C. Chen, B. Yu, P. Liu, J. Liu, L. Wang, Investigation of nano-sized ZnO particles fabricated by various synthesis routes, J. Ceram. Process. Res. 12 (2011) 420–425 doi:13.420-425.

[15] S. Liu, Y. Liu, Q. Mu, F. Zhang, H. Li, Y. Wang, Synthesis, characterization and photoluminescent properties of rare-earth hydroxides and oxides nanorods by hydrothermal route, Appl. Phys. A Mater. Sci. Process. 111 (2013) 1229–1240, https://doi.org/10.1007/s00339-012-7387-3.

[16] M. Gusatti, D.A.R. Souza, N.C. Kuhnen, H.G. Riella, Growth of variable aspect ratio ZnO nanorods by solochemical processing, J. Mater. Sci. Technol. 31 (2015) 10–15, https://doi.org/10.1016/j.jmst.2014.08.001.

[17] M. Gusatti, C.E.M. Campos, D.A.R. Souza, N.C. Kuhnen, H.G. Riella, P.S. Pizani, Effects of reaction temperature on structural properties of ZnO nanocrystals prepared via solochemical technique, J. Nanosci. Nanotechnol. 12 (2012) 7986–7992, https://doi.org/10.1166/jnn.2012.6646.

[18] M.R. Vaezi, S.K. Sadrnezhaad, Nanopowder synthesis of zinc oxide via solochemical processing, Mater. Des. 28 (2007) 515–519, https://doi.org/10.1016/j.matdes.2005.08.016.

[19] T. Shokuhfar, M.R. Vaezi, S.K. Sadrnezhad, A. Shokuhfar, Synthesis of zinc oxide nanopowder and nanolayer via chemical processing, Int. J. Nanomanuf. 2 (2008) 149, https://doi.org/10.1504/IJNM.2008.017846.

[20] Y. Cao, W. Pan, Y. Zong, D. Jia, Preparation and gas-sensing properties of pure and Nd-doped ZnO nanorods by low-heating solid-state chemical reaction, Sensors Actuators, B Chem. 138 (2009) 480–484, https://doi.org/10.1016/j.snb.2009.03.015.

[21] K. Bouras, G. Schmerber, D. Aureau, H. Rinnert, G. Ferblantier, T. Fix, S. Colis, P. Bazylewski, B. Leedahl, A. Etcheberry, G.S. Chang, A. Dinia, A. Slaoui, Insight into photon conversion of Nd^{3+} doped low temperature grown p and n type tin oxide thin films, RSC Adv. 6 (2016) 67157–67165, https://doi.org/10.1039/C6RA14460H.

[22] B. Shahmoradi, K. Soga, S. Ananda, R. Somashekar, K. Byrappa, Modification of neodymium-doped ZnO hybrid nanoparticles under mild hydrothermal conditions, Nanoscale 2 (2010) 1160, https://doi.org/10.1039/c0nr00069h.

[23] M. Azadi, A.H. Hasani, M.E. Olya, S.M. Borghei, Application of ZnO-Ag-Nd nanocomposite as a new synthesized nanophotocatalyst for the degradation of organic compounds: kinetic, thermodynamic and economic study, Toxicol. Ind. Health 35 (2019) 1–10, https://doi.org/10.1177/0748233718796720.

[24] A.S.H. Hameed, C. Karthikeyan, A.P. Ahamed, N. Thajuddin, N.S. Alharbi, S.A. Alharbi, G. Ravi, In vitro antibacterial activity of ZnO and Nd doped ZnO nanoparticles against ESBL producing Escherichia coli and Klebsiella pneumoniae, Sci. Rep. 6 (2016) 1–11, https://doi.org/10.1038/srep24312.

[25] Anindita Samanta, M.N. Goswami, P.K. Mahapatra, Influence of Nd^{3+} doping in ZnO nanoparticles to enhance the optical and photocatalytic activity, Mater. Res. Express 6 (2019), https://doi.org/10.1088/2053-1591/ab0c25.

[26] J. Sin, C. Lim, S. Lam, A.R. Mohamed, H. Zeng, Facile synthesis of novel ZnO/Nd-doped BiOBr composites with boosted visible light photocatalytic degradation of phenol, Mater. Lett. (2019), https://doi.org/10.1016/j.matlet.2019.03.129.

[27] J. Hao, X. Wang, F. Liu, S. Han, J. Lian, Q. Jiang, Facile synthesis ZnS/ZnO/$Ni(OH)_2$ composites grown on Ni foam: a bifunctional materials for photocatalysts and supercapacitors, Sci. Rep. 7 (2017) 1–12, https://doi.org/10.1038/s41598-017-03200-2.

[28] S.R. Sanivarapu, J.B. Lawrence, G. Sreedhar, Role of surface oxygen vacancies and lanthanide contraction phenomenon of $Ln(OH)_3$ (Ln = La, Pr, and Nd) in sulfide-mediated photoelectrochemical water splitting, ACS Omega 3 (2018) 6267–6278, https://doi.org/10.1021/acsomega.8b00429.

[29] Y. Wang, Y. Wang, S. Liu, Y. Cai, S. Deng, B. Han, R. Han, Q. Li, La $(OH)_3$:Ln^{3+}(Ln = Sm, Er, Gd, Dy, and Eu) nanorods synthesized by a facile hydrothermal method and their enhanced photocatalytic degradation of Congo red in the aqueous solution, Ceram. Int. 40 (2014) 5091–5095, https://doi.org/10.1016/j.ceramint.2013.09.119.

[30] Q. Gao, Y. Dai, C. Li, L. Yang, X. Li, C. Cui, Correlation between oxygen vacancies and dopant concentration in Mn-doped ZnO nanoparticles synthesized by co-precipitation technique, J. Alloys Compd. 684 (2016) 669–676, https://doi.org/10.1016/j.jallcom.2016.05.227.

[31] C. Chen, P. Liu, C. Lu, Synthesis and characterization of nano-sized ZnO powders by direct precipitation method, Chem. Eng. J. 144 (2008) 509–513, https://doi.org/10.1016/j.cej.2008.07.047.

[32] D.L. Wood, J. Tauc, Weak absorption tails in amorphous semiconductors, Phys. Rev. B 5 (1972) 3144–3151, https://doi.org/10.1103/PhysRevB.5.3144.

[33] R.G. Marques, A.M. Ferrari-Lima, V. Slusarski-Santana, N.R.C. Fernandes-Machado, Ag_2O and Fe_2O_3 modified oxides on the photocatalytic treatment of pulp and paper wastewater, J. Environ. Manage. 195 (2017) 242–248, https://doi.org/10.1016/j.jenvman.2016.08.034.

[34] J. Singh, N.S. Mishra, S. Uma, Y.C. Sharma Banerjee, Comparative studies of physical characteristics of raw and modified sawdust for their use as adsorbents for removal of acid dye, BioResources 6 (2011) 2732–2743.

[35] C. Clinical and Laboratory Standards Institute, M02-A12: Performance Standards for Antimicrobial Disk Susceptibility Tests; Approved Standard—Twelfth Edition, Clin. Lab. Stand. Inst. 35 (2015) 15. https://clsi.org/media/1631/m02a12_sample.pdf.

[36] F.R. Espinoza-quiñones, A.N. Módenes, A.R. De Pauli, S.M. Palácio, Analysis of trace elements in groundwater using ICP-OES and TXRF techniques and its compliance with brazilian protection standards, Water Air Soil Pollut. 32 (2015), https://doi.org/10.1007/s11270-015-2315-8.

[37] P.F.S. Pereira, A.F. Gouveia, M. Assis, R.C. de Oliveira, I.M. Pinatti, M. Penha, R.F. Gonçalves, L. Gracia, J. Andrés, E. Longo, $ZnWO_4$ nanocrystals: synthesis, morphology, photoluminescence and photocatalytic properties, Phys. Chem. Chem. Phys. 20 (2018) 1923–1937, https://doi.org/10.1039/C7CP07354B.

[38] R.G. Carvalho, M.T.S. Tavares, F.K.F. Oliveira, R.M. Nascimento, E. Longo, M.S. Li, C.A. Paskocimas, M.R.D. Bomio, F.V. Motta, Preparation and photocatalytic properties of hexagonal-shaped ZnO:Sm^{3+} by microwave-assisted hydrothermal method, J. Mater. Sci. Mater. Electron. 28 (2017) 7943–7950, https://doi.org/10.1007/s10854-017-6496-3.

[39] K.D. Arun Kumar, S. Valanarasu, A. Kathalingam, K. Jeyadheepan, Nd^{3+} Doping effect on the optical and electrical properties of SnO_2 thin films prepared by nebulizer spray pyrolysis for opto-electronic application, Mater. Res. Bull. 101 (2018) 264–271, https://doi.org/10.1016/j.materresbull.2018.01.050.

[40] G. Chen, Y. Wang, Q. Shen, Y. Song, G. Chen, H. Yang, Synthesis and enhanced photocatalytic activity of 3D flowerlike ZnO microstructures on activated carbon fiber, 123 (2014) 145–148.

[41] G. Byzynski, C. Melo, D.P. Volanti, M.M. Ferrer, A.F. Gouveia, C. Ribeiro, J. Andrés, E. Longo, The interplay between morphology and photocatalytic activity in ZnO and N-doped ZnO crystals, Mater. Des. 120 (2017) 363–375, https://doi.org/10.1016/j.matdes.2017.02.020.

[42] Y. Zhu, X. Zhai, L. Wang, Hydrothermal synthesis of $Ln(OH)_3$ nanorods and the conversion to LnO_3 (Ln = Eu, Nd, Dy) nanorods via annealing process, J. Nanomater. 2013 (2013) 1–7, https://doi.org/10.1155/2013/130514.

[43] C. Li, H. Liu, J. Yang, A facile hydrothermal approach to the synthesis of nanoscale rare earth hydroxides, Nanoscale Res. Lett. 10 (2015) 144, https://doi.org/10.1186/s11671-015-0850-2.

[44] S.H. Jeon, K. Nam, H.J. Yoon, Y.-I. Kim, D.W. Cho, Y. Sohn, Hydrothermal synthesis of Nd_2O_3 nanorods, Ceram. Int. 43 (2017) 1193–1199, https://doi.org/10.1016/j.ceramint.2016.10.062.

[45] J. Jalali, M. Mozammel, Degradation of water-soluble methyl orange in visible light with the use of silver and copper co-doped TiO_2 nanoparticles, J. Mater. Sci. Mater. Electron. 28 (2017) 5336–5343, https://doi.org/10.1007/s10854-016-6192-8.

[46] G.D. Dhamale, V.L. Mathe, S.V. Bhoraskar, S.N. Sahasrabudhe, S.D. Dhole, S. Ghorui, Synthesis and characterization of Nd_2O_3 nanoparticles in a radio-frequency thermal plasma reactor, Nanotechnology 27 (2016) 085603, , https://doi.org/10.1088/0957-4484/27/8/085603.

[47] S.H. Jeon, K. Nam, H.J. Yoon, Y. Il Kim, D.W. Cho, Y. Sohn, Hydrothermal synthesis of Nd_2O_3 nanorods, Ceram. Int. 43 (2017) 1193–1199, https://doi.org/10.1016/j.ceramint.2016.10.062.

[48] Z. Movasaghi, S. Rehman, I.U. Rehman, Fourier transform infrared (FTIR) spectroscopy of biological tissues, Appl. Spectrosc. Rev. 43 (2008) 134–179, https://doi.org/10.1080/05704920701829043.

[49] E. Smidt, K. Meissl, The applicability of Fourier transform infrared (FT-IR) spectroscopy in waste management, Waste Manag. 27 (2007) 268–276, https://doi.org/10.1016/j.wasman.2006.01.016.

[50] B.I., Spectrometric identification of organic compounds, 3rd edition, J. Mol. Struct. 30 (1976) 424–425. doi:10.1016/0022-2860(76)87024-X.

[51] M. Silambarasan, S. Saravanan, T. Soga, Raman and photoluminescence studies of Ag and Fe-doped ZnO nanoparticles, Int. J. ChemTech Res. 7 (2015) 1644–1650.

[52] R.C. Lima, L.R. Macario, J.W.M. Espinosa, V.M. Longo, R. Erlo, N.L. Marana, J.R. Sambrano, M.L. dos Santos, A.P. Moura, P.S. Pizani, J. Andrés, E. Longo, J.A. Varela, Toward an understanding of intermediate- and short-range defects in ZnO single crystals. A combined experimental and theoretical study†, J. Phys. Chem. A 112 (2008) 8970–8978, https://doi.org/10.1021/jp8022474.

[53] T.M. Khan, T. Bibi, B. Hussain, Synthesis and optical study of heat-treated ZnO nanopowder for optoelectronic applications, Bull. Mater. Sci. 38 (2015) 1851–1858,

https://doi.org/10.1007/s12034-015-1103-9.
[54] J.B. Gruber, D.K. Sardar, R.M. Yow, T.H. Allik, B. Zandi, Energy-level structure and spectral analysis of $Nd^{3+}(4f^3)$ in polycrystalline ceramic garnet $Y_3Al_5O_{12}$, J. Appl. Phys. 96 (2004) 3050–3056, https://doi.org/10.1063/1.1776320.
[55] J.C. Sin, S.M. Lam, K.T. Lee, A.R. Mohamed, Preparation of rare earth-doped ZnO hierarchical micro/nanospheres and their enhanced photocatalytic activity under visible light irradiation, Ceram. Int. 40 (2014) 5431–5440, https://doi.org/10.1016/j.ceramint.2013.10.128.
[56] D. Chandran, L.S. Nair, S. Balachandran, K.R. Babu, M. Deepa, Band gap narrowing and photocatalytic studies of Nd^{3+} ion-doped SnO_2 nanoparticles using solar energy, Bull. Mater. Sci. 39 (2016) 27–33, https://doi.org/10.1007/s12034-015-1142-2.
[57] L.F. Koao, B.F. Dejene, F.G. Hone, H.C. Swart, S.V. Motloung, T.E. Motaung, V.B. Pawade, Effects of octadecylammine molar concentration on the structure, morphology and optical properties of ZnO nanostructure prepared by homogeneous precipitation method, J. Lumin. 200 (2018) 206–215, https://doi.org/10.1016/j.jlumin.2018.04.024.
[58] A.A. Firooz, A.R. Mahjoub, A.A. Khodadadi, M. Movahedi, High photocatalytic activity of Zn_2SnO_4 among various nanostructures of $Zn_{2x}Sn_{1-x}O_2$ prepared by a hydrothermal method, Chem. Eng. J. 165 (2010) 735–739, https://doi.org/10.1016/j.cej.2010.09.052.
[59] N. Riaz, F.K. Chong, Z.B. Man, M.S. Khan, B.K. Dutta, Photodegradation of orange II under visible light using Cu–Ni/TiO_2: influence of Cu: Ni mass composition, preparation, and calcination temperature, Ind. Eng. Chem. Res. 52 (2013) 4491–4503, https://doi.org/10.1021/ie303255v.
[60] A.E. Pirbazari, P. Monazzam, B.F. Kisomi, Co/TiO_2 nanoparticles: preparation, characterization and its application for photocatalytic degradation of methylene blue, Desalin. Water Treat. 63 (2017) 283–292, https://doi.org/10.5004/dwt.2017.20205.
[61] S.A. Hosseini, S. Babaei, Graphene oxide/zinc oxide (GO/ZnO) nanocomposite as a superior photocatalyst for degradation of methylene blue (MB)-process modeling by response surface methodology (RSM), J. Braz. Chem. Soc. 28 (2017) 299–307, https://doi.org/10.5935/0103-5053.20160176.
[62] U.K. Sahu, S.S. Mahapatra, R.K. Patel, Application of Box-Behnken Design in response surface methodology for adsorptive removal of arsenic from aqueous solution using CeO_2/Fe_2O_3/graphene nanocomposite, Mater. Chem. Phys. 207 (2018) 233–242, https://doi.org/10.1016/j.matchemphys.2017.11.042.
[63] N. Mohaghegh, M. Tasviri, E. Rahimi, M.R. Gholami, Nano sized ZnO composites: preparation, characterization and application as photocatalysts for degradation of AB92 azo dye, Mater. Sci. Semicond. Process. 21 (2014) 167–179, https://doi.org/10.1016/j.mssp.2013.12.023.
[64] T.C. Machado, T.M. Pizzolato, A. Arenzon, J. Segalin, M.A. Lansarin, Photocatalytic degradation of rosuvastatin: analytical studies and toxicity evaluations, Sci. Total Environ. 502 (2015) 571–577, https://doi.org/10.1016/j.scitotenv.2014.09.076.
[65] R.A.C. Amoresi, R.C. Oliveira, N.L. Marana, P.B. de Almeida, P.S. Prata, M.A. Zaghete, E. Longo, J.R. Sambrano, A.Z. Simões, CeO_2 nanoparticle morphologies and their corresponding crystalline planes for the photocatalytic degradation of organic pollutants, ACS Appl. Nano Mater. (2019), https://doi.org/10.1021/acsanm.9b01452.
[66] I.M.P. Silva, G. Byzynski, C. Ribeiro, E. Longo, Different dye degradation mechanisms for ZnO and ZnO doped with N (ZnO:N), J. Mol. Catal. A Chem. 417 (2016) 89–100, https://doi.org/10.1016/j.molcata.2016.02.027.
[67] L. Zhang, L. Wu, Y. Si, K. Shu, Size-dependent cytotoxicity of silver nanoparticles to Azotobacter vinelandii: growth inhibition, cell injury, oxidative stress and internalization, PLoS One 13 (2018) e0209020, , https://doi.org/10.1371/journal.pone.0209020.
[68] Y.N. Slavin, J. Asnis, U.O. Häfeli, H. Bach, Metal nanoparticles: understanding the mechanisms behind antibacterial activity, J. Nanobiotechnol. (2017) 1–20, https://doi.org/10.1186/s12951-017-0308-z.
[69] M. Zanet, Valentina; Vidic, Jasmina; Auger, Sandrine; Vizzini, Priya; Lippe, Giovanna; Iacumin, Lucilla; Comi, Giuseppe; Manzano, Activity evaluation of pure and doped zinc oxide nanoparticles against bacterial, J. Appled Microbiol. (2019) 0–2. doi:10.1111/jam.14407.
[70] V.K.H. Bui, P. Duckshin, Y. Lee, Chitosan combined with ZnO, TiO_2 and Ag nanoparticles for antimicrobial wound healing applications: a mini review of the research trends, Polymers (Basel). 9 (2017) 1–24, https://doi.org/10.3390/polym9010021.
[71] H.M. Yusof, R. Mohamad, U.H. Zaidan, N. Aini, A. Rahman, Microbial synthesis of zinc oxide nanoparticles and their potential application as an antimicrobial agent and a feed supplement in animal industry : a review, (2019) 1–22.
[72] V. Slusarski-Santana, L.D. Fiorentin-Ferrari, M.L. Fiorese, Antimicrobial Activities of Photocatalysts for water disinfection, in: Nanophotocatalysis Environ. Appl. Detoxif. Disinfect., 2019: pp. 217–243.
[73] P.J.P. Espitia, N. de F.F. Soares, J.S. dos R. Coimbra, N.J. de Andrade, R.S. Cruz, E. A.A. Medeiros, Zinc oxide nanoparticles: synthesis, antimicrobial activity and food packaging applications, food bioprocess Technol. 5 (2012) 1447–1464. doi:10.1007/s11947-012-0797-6.
[74] T. Verdier, M. Coutand, A. Bertron, C. Roques, Antibacterial activity of TiO2 photocatalyst alone or in coatings on E. coli: the influence of methodological aspects, Coatings. 4 (2014) 670–686. doi:10.3390/coatings4030670.
[75] L.M. Gilbertson, E.M. Albalghiti, Z.S. Fishman, F. Perreault, J.D. Posner, M. Elimelech, L.D. Pfefferle, J.B. Zimmerman, L.M. Gilbertson, E.M. Albalghiti, Z.S. Fishman, D. Pfefferle, J.B. Zimmerman, Shape-dependent surface reactivity and antimicrobial activity of nano-cupric oxide shape-dependent surface reactivity and antimicrobial activity of nano-cupric oxide in preparation for submission to environmental science and technology, Environ. Sci. Technol. (2016), https://doi.org/10.1021/acs.est.5b05734.
[76] Y. Baek, Y. An, Science of the total environment microbial toxicity of metal oxide nanoparticles (CuO, NiO, ZnO, and Sb2O3) to Escherichia coli, Bacillus subtilis, and Streptococcus aureus, Sci. Total Environ. 409 (2011) 1603–1608, https://doi.org/10.1016/j.scitotenv.2011.01.014.